The Impact of Large-Scale Orography on Northern Hemisphere Winter Synoptic Temperature Variability

Nicholas J. Lutsko*

Department of Earth, Atmospheric, and Planetary Sciences, Massachusetts Institute of Technology, Cambridge, Massachusetts

Jane W. Baldwin

Princeton Environmental Institute, Princeton University, Princeton, New Jersey

Timothy W. Cronin

Department of Earth, Atmospheric, and Planetary Sciences, Massachusetts Institute of Technology, Cambridge, Massachusetts

**Corresponding author address:* Nicholas Lutsko, Department of Earth, Atmospheric, and Planetary Sciences, Massachusetts Institute of Technology, Cambridge, Massachusetts

E-mail: lutsko@mit.edu

ABSTRACT

The impact of large-scale orography on wintertime near-surface (850hPa) temperature variability on daily and synoptic time-scales (days to weeks) in the Northern Hemisphere is investigated. Using a combination of theory, idealized modeling work and simulations with a comprehensive climate model, it is shown that large-scale orography reduces upstream temperature gradients, in turn reducing upstream temperature variability, and enhances downstream temperature gradients, enhancing downstream temperature variability. Hence the presence of the Rockies on the western edge of the North American continent increases temperature gradients over North America and, consequently, increases North American temperature variability. By contrast, the presence of the Tibetan Plateau and the Himalayas on the eastern edge of the Eurasian continent damps temperature variability over most of Eurasia. However, Tibet and the Himalayas also interfere with the downstream development of storms in the North Pacific storm track, and thus damp temperature variability over North America, by approximately as much as the Rockies enhance it.

Large-scale orography is also shown to impact the skewness of downstream temperature distributions, as temperatures to the north of the enhanced temperature gradients are more positively skewed while temperatures to the south are more negatively skewed. This effect is most clearly seen in the northwest Pacific, off the east coast of Japan.

1. Introduction

Temperature variability is one of the most important features of the climate for human society and natural ecosystems, affecting, among many other things, agricultural and economic production (Lazo et al. (2011); Wheeler and von Braun (2013); Shi et al. (2015); Jahn (2015); Bathiany et al. (2018)) and the rhythms of ecological seasons (Jackson et al. (2009); Bowers et al. (2016)). Changes in temperature variability may be among the most impactful aspects of future climate change, which has motivated much recent work on the mechanisms controlling temperature variability in present and future climates, with two primary foci: *(1)* the question of how Arctic amplification will influence mid-latitude temperature variability; and *(2)* the question of what controls the zonal-mean variance and higher-order moments of the temperature distribution (e.g., Schneider et al. (2015); Garfinkel and Harnik (2017); Linz et al. (2018)). With respect to Arctic amplification, it is now clear that, in winter, mid-latitude zonal-mean temperature variance will be reduced (Screen (2014); Schneider et al. (2015); Hoskins and Woollings (2015)), though the effect of Arctic amplification on higher moments of mid-latitude temperature distributions is still uncertain (e.g., Cohen et al. (2014); Barnes and Polvani (2015)).

Little work, however, has been done to understand what controls regional (zonally-asymmetric) patterns of temperature variability, despite their societal relevance. For instance, changes in heat-waves with global warming can be well predicted by superposing a mean shift on present-day daily temperature variability, so that understanding the pattern of temperature variance is key for forecasting spatial variations in heat-wave changes with warming (Rahmstorf and Coumou (2011); Lau and Nath (2012); Lau and Nath (2014); Huybers et al. (2014); McKinnon et al. (2016)).

An example of a regional difference in temperature variability can be seen in panels a and b of Figure 1. Whether using daily data (panel a) or filtering to synoptic time-scales (days to weeks, panel b), North America experiences substantially more near-surface (850hPa) temperature variability than Eurasia during boreal winter (December-January-February, DJF, see section 2 for description of observational dataset). This is also shown by Figure 1e, which plots a longitudinal profile of DJF synoptic temperature variance at 50°N: temperature variance at this latitude is roughly twice as large over North America as over Eurasia. Investigating the contribution of large-scale Northern Hemisphere orography (Asian orography, which includes the Himalayas, the Tibetan Plateau and the Mongolian Plateau, and the Rockies) to the enhancement of temperature variability over North America compared to Eurasia is the primary goal of the present study.

Our analysis is based on the dominant control of winter synoptic temperature variability by horizontal advection, which implies in turn that mean horizontal temperature gradients, particularly meridional gradients, are the primary control on synoptic temperature variability (Schneider et al. (2015); Holmes et al. (2016); see section 3a below). It can be seen in panels c and d of Figure 1 that both zonal and meridional temperature gradients are larger over North America than over Eurasia during winter, suggesting that whatever causes these enhanced gradients is also responsible for the enhanced variability over North America. Specifically, the importance of temperature gradients for synoptic temperature variability implies a close link between the Northern Hemisphere winter stationary wave pattern and the regional distribution of winter temperature variability.

Waves forced by large-scale orography are a key component of the winter stationary wave pattern in the Northern Hemisphere (Held et al. 2002). Below, we show that orography increases downstream temperature gradients and decreases upstream temperature gradients, with corresponding impacts on temperature variability. We demonstrate this mechanism in simulations with two idealized atmospheric general circulation models (GCMs), one dry and one moist, which also allow us to investigate how the shape of the orography influences its impact on temperature variability and how moist processes impact the dynamics (section 3). We then present simulations with a comprehensive climate model in which the major Northern Hemisphere mountain ranges are flattened, to quantify the impact these have on winter temperature variability (section 4). A complicating factor is orography's effect on downstream development: the presence of large-scale orography can weaken downstream eddies by interfering with the recycling of energy from upstream, leading to reduced temperature variability far from the orography.

By enhancing and reducing mean temperature gradients, orography also impacts the skewness of temperature distributions, which we explore in section 5. We end with conclusions in section 6.

2. Data and Methods

a. Observational Data

Observational data are taken from the Modern-Era Retrospective Analysis for Research and Applications (MERRA) dataset (Rienecker et al. 2011). The MERRA grid has 1.25° resolution in latitude and longitude, and we have taken daily-averaged data from December, January and February for the years 1979 to 2012.

b. Dry GCM

The dry GCM is the GFDL spectral dynamical core, which solves the primitive equations for a dry ideal gas on the sphere, and is forced by Newtonian relaxation to a prescribed zonally-symmetric equilibrium temperature field and damped by Rayleigh friction near the surface. The parameter settings are the standard Held-Suarez parameters with forcing symmetric about the equator (Held and Suarez 1994). This set-up produces an equinoctial climate similar to that of the real atmosphere, though there are no stratospheric polar vortices due to the uniform stratospheric relaxation temperature.

As in Lutsko and Held (2016), the model is perturbed by adding a Gaussian mountain, with the form

$$h(\phi,\lambda) = H \exp\left\{-\left[\frac{(\phi-\phi_0)^2}{\alpha^2} + \frac{(\lambda-\lambda_0)^2}{\beta^2}\right]\right\}, \tag{1}$$

where H is the maximum height of the mountain in meters; λ and ϕ are longitude and latitude, respectively; λ_0 and ϕ_0 are the co-ordinates of the center of the mountain; and α and β are half-widths, both set to 15° in the main suite of simulations. λ_0 and ϕ_0 were set to 90°E and 45°N, respectively, in all simulations.

H was varied from 333m, which is in the "linear" regime, with air mostly flowing up and over the mountain, to 4km, which is in the "non-linear" regime, with air mostly deflected around that orography (Lutsko and Held 2016). In every simulation, the model was run at T85 resolution with 30 evenly spaced sigma levels, and the instantaneous wind, surface pressure and temperature fields were sampled once per day. We present results from simulations lasting 5000 days, with data taken from the final 4000 days.

c. Moist GCM

The moist GCM is the gray-radiation model first described by Frierson et al. (2006), though we have used the parameter settings of O'Gorman and Schneider (2008), and also included their parameterization of short-wave absorption by the atmosphere. The model uses the GFDL spectral dynamical core, and includes the simplified Betts-Miller (SBM) convection scheme of Frierson (2007). We show results using a convective relaxation time-scale τ_{SBM} of 2 hours and a reference relative humidity RH_{SBM} = 0.7. The boundary layer scheme is the one used by O'Gorman and Schneider (2008). The moist GCM is run under perpetual equinox conditions, with no daily cycle of insolation, and is coupled to a slab ocean of depth 1m, with no representation of ocean dynamics or of sea ice. A mixed-layer depth of 1m was used so that the model would spin up quickly; using a deeper mixed-layer damps the temperature variance, but otherwise our results are qualitatively insensitive to the choice of mixed-layer depth. Moreover, a mixed-layer depth of 1m allows surface temperatures to respond to synoptic-scale forcing, as continental land surfaces do. A deeper mixed-layer depth, more representative of an oceanic mixed-layer, would decouple surface temperatures from synoptic temperature variability.

The same Gaussian orography is added to the model as in the dry GCM, except that it is centered further north at 60°N. The reason for moving the orography poleward is that the storm tracks, and the associated maxima in temperature variance, are further poleward in this set-up (see Figure 3 below), so a more northward mountain produces clearer changes in variance. As discussed by Wills and Schneider (2018), this implementation of orography produces an "aqua-mountain", and the surface fluxes over the orography are not necessarily realistic. However, any bias in the surface fluxes is of secondary importance for our investigation.

The moist GCM was integrated at T85 truncation with 30 unevenly-spaced vertical levels, starting from a state with uniform SSTs. The simulations lasted for 4500 days with data stored four times per day, and we have taken averages over the final 4000 days.

Our focus in this study is on winter temperature variability, as land surface processes, like soil-moisture feedbacks, are less important for variability in winter than in summer. As neither of the idealized GCMs includes a representation of land surface processes, they can be used to study the mechanisms of winter temperature variance without imposing seasonality and so, for convenience, we have used set-ups that produce equinoctial climates.

d. Comprehensive climate model

The comprehensive climate model is GFDL CM2.5-FLOR (Vecchi et al. 2014). FLOR stands for Forecast-oriented Low Ocean Resolution, and the model is based on the GFDL CM2.5 model. It is run with an atmospheric resolution of approximately 50km and an oceanic resolution of approximately 1°. By running with a relatively high resolution atmosphere, FLOR is able to accurately capture many subseasonal forms of variability, such as hurricanes and monsoon depressions, and can resolve sharp topographic features, such as the peaks of the Himalayas (compare panels a and b of Figure 2).

Three simulations were performed with FLOR: *(1)* a control simulation with present-day topography, *(2)* a simulation with the Rockies flattened to 300m (the "no-Rockies" simulation, i.e., all surface heights greater than 300m are reduced to 300m) and *(3)* a simulation with the Asian orography (the Tibetan Plateau, the Himalayas and the Mongolian Plateau) flattened to 300m (the "no-Tibet" simulation). The regions of flattened topography can be seen in Figure 2 and we note that the gravity wave drag and boundary layer roughness were fixed to their control values where the topography was flattened (see also Baldwin et al. (2019b)).

All simulations were conducted with pre-industrial radiative forcings, matching the best guess for the year 1860, and with static vegetation. Daily-mean data were collected for 50 years, following 100 years of spin-up from an initial state of rest, and SSTs were relaxed to a repeating climatology with a relaxation time-scale of five days. This set-up was originally designed to allow tropical cyclones to interact with the ocean surface (Vecchi et al. 2014); for our purposes, the model is essentially an atmosphere-only climate model run over fixed SSTs. Our configuration attempts to isolate the direct effects of the orographic forcing on temperature variability, though not the indirect effects orography has on variability through its impact on SSTs.

e. Filtering to synoptic time-scales

The data were filtered to synoptic time-scales using a fourth-order Butterworth filter, with cut-off frequencies of 1/3 days^{-1} and 1/15 days^{-1}. The filter was implemented using the Python package `scipy.signal`, with the filter co-efficients obtained using `scipy.signal.butter` and the filtering done with `scipy.signal.lfilter`. We have verified that our results are robust to the choice of filtering time-scales, within reason. For all datasets, DJF variance and skewness were calculated individually for each year (e.g., December 1979 to February 1980) and then averaged over all years to find the climatological variance and skewness.

3. Impact of Orography on Temperature Variance in Idealized Models

a. Background theory

Assuming that synoptic potential temperature variations are primarily generated by horizontal advection, and that this advection is local in time and space, potential temperature variations can be Taylor expanded to give (Corrsin (1974); Schneider et al. (2015))

$$\theta' \approx -\frac{\partial \bar{\theta}}{\partial y} L_y' - \frac{\partial \bar{\theta}}{\partial x} L_x' + \frac{1}{2}\frac{\partial^2 \bar{\theta}}{\partial y^2} L_y'^2 + ..., \tag{2}$$

where $\theta' = \theta - \bar{\theta}$ denotes synoptic variations of potential temperature at 850hPa about some local mean value $\bar{\theta}$, L_y' is the Lagrangian displacement of air masses arriving at y from y_0, and similarly for L_x'. "Mean" denotes an average over a time-scale that is long compared to synoptic time-scales and we consider potential temperature rather than temperature because potential temperature is materially conserved during adiabatic airmass displacements. We work in Cartesian co-ordinates for simplicity, and define L_y' as positive for a northward displacement and L_x' as positive for an eastward displacement. Provided the length scales of potential temperature variations, $\overline{L_y} = 2|\partial_y \bar{\theta}/\partial_{yy}\bar{\theta}|$ and $\overline{L_x} = 2|\partial_x \bar{\theta}/\partial_{xx}\bar{\theta}|$, are much larger than the mixing length-scales, L_y' and L_x', the expansion can be well approximated by just retaining the first two terms, and so the synoptic potential temperature variance can be approximated as

$$\overline{\theta'^2} \approx \overline{\left(\frac{\partial\bar{\theta}}{\partial y}\right)^2 L_y'^2} + \overline{\left(\frac{\partial\bar{\theta}}{\partial x}\right)^2 L_x'^2} + 2\,\overline{\left(\frac{\partial\bar{\theta}}{\partial y}\right) L_y' \left(\frac{\partial\bar{\theta}}{\partial x}\right) L_x'}. \tag{3}$$

The meridional term, specifically the meridional temperature gradient, generally dominates over the zonal term and the cross term (note the different colorbar scales in panels c and d of Figure 1), but we have included the latter two here to emphasize that zonal temperature gradients also impact regional potential temperature variability.

Orography affects temperature gradients by meridionally compressing downstream near-surface isentropes and pulling apart upstream isentropes. However, this requires the flow to be deflected around the orography, rather than flowing up and over it, so that the air deflected equatorward partly adjusts to the warmer conditions and the air deflected poleward partly adjusts to the colder conditions, before the downstream confluence of the flow. For small heights the air flows up and over the orography, leaving the potential temperature gradients unaffected. Formally, consider the linearized, time-mean thermodynamic equation for adiabatic flow on the lowest model level (in z coordinates):

$$\bar{u}\frac{\partial\theta'}{\partial x} + v'\frac{\partial\bar{\theta}}{\partial y} = -w\frac{\partial\bar{\theta}}{\partial z}. \tag{4}$$

The orographic forcing enters through the lower boundary condition, which can be approximated in the linear regime as (Cook and Held 1992)

$$w \approx \bar{u}\frac{\partial h}{\partial x}, \tag{5}$$

where h is again the height of the orography, with maximum height H. Substituting then gives

$$\bar{u}\frac{\partial\theta'}{\partial x} + v'\frac{\partial\bar{\theta}}{\partial y} = -\bar{u}\frac{\partial h}{\partial x}\frac{\partial\bar{\theta}}{\partial z}. \tag{6}$$

In this linear regime, the air moves up and over the mountain, and the first term on the left side of equation 6 balances the right side so that $\frac{\theta'}{H} \sim \frac{\partial\bar{\theta}}{\partial z}$. For larger H the flow becomes increasingly non-linear, and the deflection around the orography is important. In this regime the forcings associated with the meridional wind and with zonal wind anomalies can no longer be ignored in equation 5, and the orographic forcing is balanced by the $v'\frac{\partial\bar{\theta}}{\partial y}$ term[1]. In idealized experiments this transition occurs for H between 1 and 2km for orography with approximately the same horizontal extent as the Tibetan Plateau (Cook and Held (1992), Lutsko and Held (2016)). Valdes and Hoskins (1991) demonstrated that Asian topography meets this criterion, but caution that it is less clear whether the Rockies do, with the result depending on how the Rockies are defined. Furthermore, while the near-surface flow appears to be deflected around the Rockies (see Figure 9 below), this flow is strongly influenced by heating in the north Pacific storm track (see also Valdes and Hoskins (1989)).

Another factor which enhances the downstream temperature gradients is the preferential deflection of the flow around the poleward side of the orography. If the flow follows isentropes, then it will descend in height when it moves equatorward and ascend in height when it moves poleward, following the mean isentropic slope (Valdes and Hoskins 1991). Thus the mountain appears "taller" to the flow on its equatorward flank and "shorter" on its poleward flank, so that more of the air flows around the poleward flank of the mountain. The downstream convergence is then equatorward of the center of the orography, with anomalously cold air meeting the warm air that flowed around the equatorward side of the orography.

---

[1]Though note that the potential temperature perturbation is itself proportional to the deflection of the flow: $\theta' \approx \eta'\frac{\partial\bar{\theta}}{\partial y}$, where η is the typical meridional displacement of a fluid parcel, assumed to be equal to the meridional extent of the orography. Hence the condition for meridional deflection to dominate is $|\eta/H| < \left|\frac{\partial\bar{\theta}}{\partial z}/\frac{\partial\bar{\theta}}{\partial y}\right|$. Roughly, the meridional slope of the mountain must be greater than the characteristic slope of the isentropes (Valdes and Hoskins 1991).

b. Idealized GCM results

In both idealized GCMs, temperature variance is reduced upstream and enhanced downstream of orography (Figure 3a and b), as are meridional temperature gradients (panels c and d). However the inferred mixing lengths $L' = \sqrt{\theta'^2 / \left(\frac{\partial\bar{\theta}}{\partial y}\right)^2}$ are reduced downstream of the orography (panels e and f), which is the result of two competing effects. First, by increasing downstream temperature gradients, orography increases downstream Eady growth rates, potentially leading to more energetic eddies and thus to larger mixing lengths (see Caballero and Hanley (2012) for discussion of the relationship between eddy kinetic energy and mixing lengths). But in addition to local baroclinicity, eddies in strong jets are also energized by downstream development – by the recycling of energy from upstream eddies (Chang and Orlanski (1993); Chang et al. (2002)). Orography disrupts the latter by interfering with the zonal propagation of wave packets (Son et al. 2009), and for the set-ups used here this effect wins out, resulting in less energetic eddies and smaller effective mixing lengths. This reduction in the mixing lengths has a substantial impact on the local response of the variance. For instance, panel a of Figure 4 shows the zonal anomalies in synoptic temperature variance for the simulation with the dry GCM and H = 4km, and it can be seen that the reduction in the mixing lengths creates a small region, near 120°E, in which the downstream variance is reduced, while the largest increase in variance is further downstream, at around 170°E, where the eddies are more energetic.

On the poleward side of the mountain the pattern is reversed (Figure 4a), with enhanced temperature variance upstream and reduced variance downstream of the mountain. This is partly caused by the preferential deflection of the flow around the poleward flank of the mountain (arrows in Figure 3a), which induces convergence on the northwest flank of the mountain, and thus a tightening of the isentropes, and divergence on the northeast flank of the mountain, causing the isentropes to pull apart (see contours in Figure 3c). The jet is also relatively narrow in the dry GCM, compared to typical winter climates, so that there are strong polar easterlies at the latitudes of the poleward edge of the mountain. Hence the northeast flank is upstream of the mountain, and temperature variance should be reduced there.

Our focus is on the jet regions, however, where the enhanced meridional temperature gradients cause a local enhancement of temperature variance downstream of the orography in both models. Figure 5 shows that the maximum zonal anomaly in potential temperature variance increases in the simulations with the dry and moist GCMs as the height of the orography (H) is increased (panel a)[2], as does the maximum zonal anomaly of the squared meridional temperature gradient (panel b). Plotting these against each other demonstrates the strong linear relationship between the two quantities in the GCMs (panel c). The different slopes indicate that the mixing lengths differ in the two models, and the larger slope for the moist GCM implies that adding moist processes increases the effective mixing length (see below).

A possible complication is the shape of the orography: the Rockies form a meridionally-elongated ridge, whereas the Himalayas are more zonally-elongated. To investigate how the orography's shape influences temperature variability, two additional simulations were run with the dry GCM, one with a 4km meridional ridge resembling the Rockies ($\alpha = 15^\circ$ and $\beta = 5^\circ$) and one with a 4km zonal ridge ($\alpha = 5^\circ$ and $\beta = 15^\circ$).

Panels b and c of Figure 4 show the zonal anomalies in temperature patterns in these simulations (we note that the zonal-mean variance is lower in both of the ridge experiments than in the circular experiment because the ridges interfere less with the downstream development and hence the mixing lengths are larger than in the circular experiment). The zonal anomalies are broadly similar in

[2]Note that the zonal-mean variance decreases with increasing H in both models because of the increasing disruption of downstream development by the orography (not shown).

all three experiments, with reductions in temperature variance upstream of the mountains and enhancements downstream of the mountain and a reversed pattern at higher latitudes, however there are some noticeable differences. For instance, in the zonal ridge case the reduction is mostly on the southern flank of the mountain, rather than to the southwest. The meridional ridge produces a similar response to the circular experiment, but a key difference is that the variance is increased on the entire eastern flank of the meridional ridge. The Rockies show a similar local enhancement of variance on their eastern flank (Figure 1). In the meridional ridge simulation the largest increase in variance is also immediately downstream of the orography, on its southeastern flank, instead of being displaced further downstream, as for the circular case. Decomposing this response into a squared gradient and an inferred mixing length shows that in the meridional ridge case the temperature gradient is more strongly increased immediately downstream of the orography, relative to the reduction in the mixing length (not shown).

In the dry GCM, advection is the sole method of generating potential temperature variance, whereas in the moist GCM covariance of anomalous latent heating and potential temperature anomalies also contributes. To investigate the role of latent heat anomalies, Figure 6 shows the advective terms in the temperature variance budget (see equation 3 of Wilson and Williams (2006)) for the $H = 4$km simulation with the moist GCM, as well as the contribution of latent heat fluctuations to temperature variance ($\overline{\theta' Q_L'}$, Figure 6d). Latent heating enhances temperature variability downstream of the orography, increasing the inferred mixing lengths diagnosed in the moist GCM and partly explaining why the downstream maximum in temperature variability is closer to the mountain in this GCM than in the dry GCM. This enhancement is around 20% of the advective tendency, which is dominated by the $\overline{\mathbf{u}'\theta'} \cdot \nabla\bar{\theta}$ term, and comes about because the latent heating fluctuations are related to the advection. For instance, anomalously warm air, originating close to the surface in the tropics, will condense water as it moves poleward and rises, further enhancing the temperature anomalies.

In summary, the results of the GCM simulations agree with the theoretical expectations from the previous section, with reductions and enhancements of temperature variance caused mostly by changes in meridional temperature gradients due to the presence of orography. This is complicated, however, by reductions in the effective mixing lengths due to the interference of the orography with downstream development. The ridge experiments with the dry GCM also demonstrated important dependencies on the aspect ratio of the orography. In the case of a meridional ridge, resembling the Rockies, the variance is enhanced immediately downstream of the orography, whereas with a more "circular" orography the largest enhancement is further downstream. Finally, analyzing the temperature variance of the moist GCM demonstrates that the contribution of latent heating anomalies to temperature variance enhances the variance due to horizontal advection, as these latent heating anomalies are tied to the advection itself. So we can proceed by focusing on the advection, noting that latent heating enhances the effective mixing lengths.

4. Temperature Variability in Simulations with Flattened Orography

Figure 7a shows that FLOR is able to reproduce the main features of MERRA's pattern of DJF synoptic temperature variance[3]. In Figure 7b it can be seen that the effect of the Asian orography is to decrease the temperature variance over most of Eurasia, as well as over the North Pacific and North America, and to increase the variance over central Siberia (see also Figure 8). Notably, temperature variance is reduced over the heavily populated southeast Asian coast, including southern China, in the control simulation compared to the no-Tibet simulation. In part, this is because at

[3]The temperature variance is somewhat higher in the FLOR simulations than in the reanalysis, which we attribute in part to the higher resolution of FLOR's atmospheric model compared to the reanalysis: coarse-graining the data from the control simulation to a 1.25° grid reduces the synoptic temperature variance by about 30% on average (not shown). See also Supplementary Figure 3 of Baldwin et al. (2019a).

these latitudes the zonal-winds transition from westerly to easterly and this region is upstream of the orography (Figure 9). However, the primary cause of the reduced variance is the Asian orography's interference with downstream development, which weakens the storms over southeast Asia and, especially, in the Pacific storm track (Figure 10c). The Kuroshio Extension off the east coast of Japan is the genesis region for the Pacific storm track, and the Himalayas and Tibet weaken the eddies formed over the Kuroshio because of the reduced energy from upstream, despite the increased temperature gradient in the northwest Pacific. The reduced downstream development also impacts the strength of winter storms originating in the Pacific storm track and reaching North America.

The winter stationary wave pattern over Eurasia consists of a zonally oriented dipole, with anomalous warmth over Europe and anomalous cold over east Asia (Figure 7g). The presence of Tibet cools east Asia (compare Figure 7 panels g and h), implying that the stationary wave forced by the Asian orography constructively interferes with the stationary wave excited by the land-sea contrast on Eurasia's east coast (Kaspi and Schneider (2011); Park et al. (2013)). In the absence of the Asian orography the largest Eurasian temperature gradients are at relatively low latitudes, with the maximum gradient at about 30°N (Figure 7e), whereas the mid-latitude jet, where the mixing lengths are largest, is further north. This southward displacement of the maximum temperature gradient when the orography is flattened contributes to the smaller temperature variance over Eurasia compared to North America in the no-Tibet simulation.

The Rockies act to increase the variance over most of North America, but also decrease the variance off the west coast of North America (panel c of Figure 7, Figure 8). Both the Rockies and the Asian orography increase the temperature variance over the polar regions, because their presence cools the high latitudes, increasing the zonal-mean equator-to-pole temperature gradient (Figure 10a). We have not fully diagnosed the reasons for this, but note that the mid-latitude jets weaken in the presence of the mountain ranges, resulting in weaker poleward transient eddy heat fluxes (Figure 10 panels b and c).

Table 1 quantifies the changes in temperature variance over the two continents by comparing DJF synoptic temperature variance in the three FLOR simulations over a Eurasian box (40°-120°E and 30°-75°N) and over a North American box (240°-280°E and 30°-75°N). The areas of the Asian mountains and the Rockies are masked whenever an average is taken over these boxes. Asian orography reduces the variance over the Eurasian box by $1.4K^2$ and over the North American box by $1.3K^2$, with both of these changes statistically significant at the 95% level based on a two-sided Student's t-test. The Rockies enhance the variance over the North American box by $1.3K^2$ and over Eurasia by $0.2K^2$, though only the change over North America is statistically significant in this case.

These calculations suggest that the enhancement of North American temperature variability by the Rockies is roughly canceled by the damping of variability due to Asian orography. The increases and decreases in variance are sensitive to the definitions of the boxes, however, and this cancellation also assumes the effects of flattening the mountain ranges individually can be linearly added together. Regardless, the majority of the orography's net effect comes from the reduction of Eurasian temperature variability by the Asian mountains and, in FLOR, this explains about a quarter of the difference in variance over the two continents ($1.4K^2$ / $5.5K^2 \approx 25\%$).

Our framework for explaining differences in temperature variance is based on differences in mean temperature gradients, which are in turn controlled by the Northern Hemisphere stationary wave pattern. So the remaining difference in temperature variance between the two continents can largely be attributed to stationary waves forced by diabatic heating, which, together with orography are responsible for the bulk of the Northern Hemisphere stationary wave pattern (Held et al. 2002).

Even in the no-Rockies simulation there are substantial meridional temperature gradients over North America (Figure 7f), and the stationary wave pattern over North America is similar in all three simulations, consisting of a dipole with anomalously warm temperatures off the west coast of North America and anomalously cold temperatures centered over northeast Canada (Figure 7 panels g), h) and i)). The dipole is weaker in the no-Rockies simulation, indicating that the stationary wave forced by the Rockies constructively interferes with the dipole. In this case, the pattern over North America is a combination of the stationary wave forced by the land-sea contrast between the east coast of North America and the western Atlantic (Kaspi and Schneider 2011), which cools eastern North America, and stationary waves forced by diabatic heating in the Pacific warm pool region and by thermal forcing in the extratropical Pacific (Hoskins and Karoly (1981); Valdes and Hoskins (1991); Held et al. (2002)). The latter includes the forcing due to the warm waters of the Kuroshio as well as the eddy sensible heat flux convergence in the Pacific storm track, making it difficult to separate out the relative contributions of the different thermal forcings.

5. Temperature Skewness

Through its effects on temperature gradients, orography also impacts the skewness of synoptic temperatures. Garfinkel and Harnik (2017) showed that, in mid-latitudes, synoptic temperature extremes occur when air is advected over regions with large mean meridional temperature gradients, so that temperatures poleward of these regions tend to be positively skewed and temperatures equatorward of these regions tend to be negatively skewed. By strengthening downstream temperature gradients, orography increases the positive skewness to the north of these gradients and the negative skewness to the south. This is illustrated in Figure 11, which shows maps of skewness in simulations with the two idealized GCMs, as well as the meridional temperature gradients. In both cases, downstream temperatures are skewed more positively north of the enhanced temperature gradients and more negatively to the south of the gradients.

In the reanalysis data, the strongest DJF meridional temperature gradients are found in the storm track regions of the west Pacific and the west Atlantic (Figure 1c). Panel a of Figure 12 shows that synoptic temperatures are positively skewed in the northwest Pacific and the northwest Atlantic, and negatively skewed to the south of these regions. The same patterns are seen in the control simulation with FLOR (Figure 12b, note that as with the variance, we attribute the larger values of skewness in part to FLOR's higher resolution). The temperature gradient in the west Pacific is reduced in the no-Tibet simulation, and comparing panels b and c of Figure 12 confirms that the skewness in the northwest Pacific is also reduced in this simulation. Averaging over the region 35°N-50°N and 140°E to 180°E (green box in Figure 12b) gives a reduction in skewness of 31% (= (0.234 - 0.162) / 0.234, difference significant at the 90% level) in the northwest Pacific.

Flattening the Rockies does not appear to affect temperature gradients in the west Atlantic (Figure 7f), and the skewness in the northwest Atlantic is comparable in the control and the no-Rockies simulations. Over land, DJF synoptic temperatures are negatively skewed at almost all latitudes, and other factors, such as land-surface feedbacks, are likely important for generating extreme events.

6. Conclusion

In this study we have investigated the contribution of large-scale orography to the increased wintertime near-surface daily and synoptic temperature variability over North America compared to Eurasia. Our analysis combines theoretical arguments, simulations with two idealized GCMs and simulations with a comprehensive climate model – GFDL CM2.5-FLOR – in which the Rockies and the Asian orography are separately flattened. These allow us to quantify the impacts these mountain ranges have on temperature variability over North America and Eurasia, and suggest that large-scale Northern Hemisphere orography is responsible for roughly 25% of the difference in variability.

Large-scale orography enhances downstream temperature variability by meridionally compressing downstream isentropes and reduces upstream temperature variability because upstream isentropes are pulled apart. At the same time, the preferential deflection of the flow towards the poleward flank of the orography, together with the presence of high latitude easterlies, can cause this pattern to be reversed at high latitudes, with enhanced variance on the northwest flank and reduced variance on the northeast flank of the orography (in the Northern Hemisphere). We have also shown that the orography's aspect ratio can cause substantial differences in the pattern of variability; for instance, a meridional ridge, resembling the Rockies, induces a stronger local enhancement of temperature variance on its downstream flank, whereas for circular orography the enhanced variance is further downstream. Finally, latent heat anomalies reinforce temperature anomalies created by advection, as anomalously warm air originating from low latitudes condenses water as it moves poleward and rises.

Most of North America is downstream of the Rockies, so wintertime temperature variability is enhanced there, while the Asian orography is on the eastern edge of Eurasia, so temperature variability is damped over most of Eurasia. An important exception is the southeast Asian littoral, which is east of the orography but exhibits reduced temperature variability due to the Asian mountains. This is partly because these regions are at latitudes of mean easterlies, or in the transition from mean westerlies to mean easterlies, and hence are upstream of the Himalayas. Another factor is interference by the Asian orography with the energization of eddies over the Asian continent and the Pacific storm track by downstream development. This results in weaker winter storms and reduced variability over the east Asian coast, the Pacific and North America. The reduction in variability over North America due to the presence of the Asian orography is approximately as large as the increase due to the presence of the Rockies.

Orography also enhances downstream skewness, as regions to the north of the enhanced temperature gradient have more positively skewed temperatures and regions to the south have more negatively skewed temperatures. In the FLOR simulations, the Himalayas and the Tibetan Plateau are found to increase temperature skewness in the northwest Pacific by about 30%.

The remaining difference in synoptic temperature variability over North America compared to Eurasia is primarily due to a combination of diabatic heating in the Pacific warm pool region, air-sea fluxes over the warm Kuroshio current and eddy sensible heat flux convergence in the Pacific storm track (Valdes and Hoskins (1989); Held et al. (2002)). The smaller width of the North American continent and its northwest-southeast sloping western coastline may also be important – Brayshaw et al. (2009) explored how this influences the North Atlantic storm track. Separating out these different factors, and the non-linear interactions between them, is an important next step.

The dominant control of horizontal advection on winter synoptic temperature variability is a powerful tool for understanding the regional pattern of temperature variability, in today's climate and how it may change in the future. This simplifies the problem to understanding the boreal winter stationary wave pattern, for which there is a large body of literature that can be drawn on (e.g., Hoskins and Karoly (1981); Held (1983); Held et al. (2002)), though differences in mixing lengths, for instance due to orographic interference with downstream development, are an important caveat. Similarly, past and future changes in temperature variability can potentially be tied to changes in the stationary wave pattern (see e.g., Löfverström et al. (2014) and Simpson et al. (2016) for investigations of past and future changes in Northern Hemisphere stationary waves). More work is needed to better understand the impact of orography on mixing lengths, as well as to account for land surface processes such as soil-moisture, which affect temperature variability, particularly during summer. These factors are also important for temperature extremes, particularly over land, where winter temperatures at almost all latitudes are negatively skewed. Nevertheless, the basic dynamics we describe here are robustly seen in idealized GCMs and in comprehensive climate models, and provide an important first step in explaining why North America experiences more wintertime temperature variability than Eurasia.

Acknowledgment. We thank Daniel Koll, Rodrigo Caballero and Gabriel Vecchi for helpful conversations over the course of this work. The manuscript was much improved by comments from three anonymous reviewers, as well as feedback from Daniel Koll and Paul O'Gorman on earlier drafts. Gabriel Vecchi kindly provided the computational resources to perform the FLOR simulations. This work was partly supported by NSF grant AGS-1623218, "Collaborative Research: Using a Hierarchy of Models to Constrain the Temperature Dependence of Climate Sensitivity".

References

Baldwin, J. W., J. B. Dessy, G. A. Vecchi, and M. Oppenheimer, 2019a: Temporally compound heat wave events and global warming: An emerging hazard. *Earth's Future*, **7**.

Baldwin, J. W., G. A. Vecchi, and S. Bordoni, 2019b: The ocean-mediated influence of asian orography on tropical precipitation and cyclones. *Climate Dynamics*, 1–20.

Barnes, E. A., and L. M. Polvani, 2015: Cmip5 projections of arctic amplification, of the north american/north atlantic circulation, and of their relationship. *Journal of Climate*, **28 (3)**, 5254–5271.

Bathiany, S., V. Dakos, M. Scheffer, and T. M. Lenton, 2018: Climate models predict increasing temperature variability in poor countries. *Science Advances*, **4 (5)**.

Bowers, E. K., J. L. Grindstaff, S. S. Soukup, N. E. Drilling, K. P. Eckerle, S. K. Sakaluk, and C. F. Thompson, 2016: Spring temperatures influence selection on breeding date and the potential for phenological mismatch in a migratory bird. *Ecology*, **97**, 2880–2891.

Brayshaw, D. J., B. Hoskins, and M. Blackburn, 2009: The basic ingredients of the north atlantic storm track. part i: Landsea contrast and orography. *Journal of the Atmospheric Sciences*, **66 (23)**, 2539–2558.

Caballero, R., and J. Hanley, 2012: Midlatitude eddies, storm-track diffusivity, and poleward moisture transport in warm climates. *Journal of the Atmospheric Sciences*, **69 (630)**, 3237–3250.

Chang, E. K. M., S. Lee, and K. L. Swanson, 2002: Storm track dynamics. *Journal of Climate*, **15 (16)**, 2163–2183.

Chang, E. K. M., and I. Orlanski, 1993: On the dynamics of a storm track. *Journal of the Atmospheric Sciences*, **50 (56)**, 999–1015.

Cohen, J., and Coauthors, 2014: Recent arctic amplification and extreme mid-latitude weather. *Nature Geoscience*, **7**, 627–637.

Cook, K. H., and I. M. Held, 1992: The stationary response to large-scale orography in a general circulation model and a linear model. *Journal of the Atmospheric Sciences*, **49 (6)**, 525–539.

Corrsin, S., 1974: Limitations of gradient transport models in random walks and in turbulence. *Advances in Geophysics*, **18A**, 25–60.

Frierson, D. M. W., 2007: The dynamics of idealized convection schemes and their effect on the zonally averaged tropical circulation. *Journal of the Atmospheric Sciences*, **64 (23)**, 1959–1976.

Frierson, D. M. W., I. M. Held, and P. Zurita-Gotor, 2006: A gray-radiation aquaplanet moist gcm. part i: Static stability and eddy scales. *Journal of the Atmospheric Sciences*, **63 (23)**, 2548–2566.

Garfinkel, C. I., and N. Harnik, 2017: The non-gaussianity and spatial asymmetry of temperature extremes relative to the storm track: The role of horizontal advection. *Journal of Climate*, **30**, 445–464.

Held, I. M., 1983: Stationary and quasi-stationary eddies in the extratropical troposphere: theory. *Large-scale Dynamical Processes in the Atmosphere*, B. J. Hoskins, and R. P. Pearce, Eds., Academic Press, New York, NY.

Held, I. M., and M. J. Suarez, 1994: A proposal for the intercomparison of the dynamical cores of atmospheric general circulation models. *Bulletin of the American Meteorological Society*, **75 (10)**, 1825–1830.

Held, I. M., M. Ting, and H. Wang, 2002: Northern winter stationary waves: Theory and modeling. *Journal of Climate*, **15 (16)**, 2125–2144.

Holmes, C. R., T. Woollings, E. Hawkins, and H. de Vries, 2016: Robust future changes in temperature variability under greenhouse gas forcing and the relationship with thermal advection. *Journal of Climate*, **29 (29)**, 2221–2235.

Hoskins, B., and T. Woollings, 2015: Persistent extratropical regimes and climate extremes. *Current Climate Change Reports*, **1 (3)**, 115–124.

Hoskins, B. J., and D. J. Karoly, 1981: The steady linear response of a spherical atmosphere to thermal and orographic forcing. *Journal of the Atmospheric Sciences*, **38 (6)**, 1179–1196.

Huybers, P., K. A. McKinnon, A. Rhines, and M. Tingley, 2014: U.s. daily temperatures: The meaning of extremes in the context of nonnormality. *Journal of Climate*, **27**, 7368–7384.

Jackson, S. T., J. L. Betancourt, R. K. Booth, and S. T. Gray, 2009: Ecology and the ratchet of events: Climate variability, niche dimensions, and species distributions. *Proceedings of the National Academy of Sciences*, **106**, 19 685–19 692.

Jahn, M., 2015: Economics of extreme weather events: Terminology and regional impact models. *Weather and Climate Extremes*, **10**, 29 – 39.

Kaspi, Y., and T. Schneider, 2011: Winter cold of eastern continental boundaries induced by warm ocean waters. *Nature*, **472**, 621–624.

Lau, N.-C., and M. J. Nath, 2012: A model study of heat waves over north america: Meteorological aspects and projections for the twenty-first century. *Journal of Climate*, **25**, 4761–4784.

Lau, N.-C., and M. J. Nath, 2014: Model simulation and projection of european heat waves in present-day and future climates. *Journal of Climate*, **27**, 3713–3730.

Lazo, J. K., M. Lawson, P. H. Larsen, and D. M. Walkman, 2011: U.s. economic sensitivity to weather variability. *Bulletin of the American Meteorological Society*, **92 (29)**, 709–720.

Linz, M., G. Chen, and Z. Hu, 2018: Large-scale atmospheric control on non-gaussian tails of midlatitude temperature distributions. *Geophysical Research Letters*, **45 (15)**, 9141–9149.

Löfverström, M., R. Caballero, J. Nilsson, and J. Kleman, 2014: Evolution of the large-scale atmospheric circulation in response to changing ice sheets over the last glacial cycle. *Climate of the Past*, **10 (4)**, 1453–1471.

Lutsko, N. J., and I. M. Held, 2016: The response of an idealized atmosphere to orographic forcing: Zonal versus meridional propagation. *Journal of the Atmospheric Sciences*, **73 (9)**, 3701–3718.

McKinnon, K. A., A. Rhines, M. Tingley, and P. Huybers, 2016: The changing shape of northern hemisphere summer temperature distributions. *Journal of Geophysical Research: Atmospheres*, **121**, 8849–8868.

O'Gorman, P. A., and T. Schneider, 2008: The hydrological cycle over a wide range of climates simulated with an idealized gcm. *Journal of Climate*, **21 (15)**, 3815–3832.

Park, H.-S., S.-P. Xie, and S.-W. Son, 2013: Poleward stationary eddy heat transport by the tibetan plateau and equatorward shift of westerlies during northern winter. *Journal of the Atmospheric Sciences*, **70 (23)**, 3288–3301.

Rahmstorf, S., and D. Coumou, 2011: Increase of extreme events in a warming world. *Proceedings of the National Academy of Sciences*, **108 (44)**, 17 905–17 909.

Rienecker, M. M., and Coauthors, 2011: Merra: Nasa's modern-era retrospective analysis for research and applications. *Journal of Climate*, **24**, 3624–3648.

Schneider, T., T. Bischoff, and H. Plotka, 2015: Physics of changes in synoptic midlatitude temperature variability. *Journal of Climate*, **28 (6)**, 2312–2331.

Screen, J. A., 2014: Arctic amplification decreases temperature variance in northern mid- to high-latitudes. *Nature Climate Change*, **4**, 577–582.

Shi, L., I. Kloog, A. Zanobetti, P. Liu, and J. D. Schwartz, 2015: Impacts of temperature and its variability on mortality in new england. *Nature Climate Change*, **5**, 988–991.

Simpson, I. R., R. Seager, M. Ting, and T. A. Shaw, 2016: Causes of change in northern hemisphere winter meridional winds and regional hydroclimate. *Nature Climate Change*, **6**, 65–70.

Son, S.-W., M. Ting, and L. M. Polvani, 2009: The effect of topography on storm-track intensity in a relatively simple general circulation model. *Journal of the Atmospheric Sciences*, **66 (23)**, 393–311.

Valdes, P. J., and B. J. Hoskins, 1989: Linear stationary wave simulations of the time-mean climatological flow. *Journal of the Atmospheric Sciences*, **46 (18)**, 2509–2527.

Valdes, P. J., and B. J. Hoskins, 1991: Nonlinear orographically forced planetary waves. *Journal of the Atmospheric Sciences*, **48 (18)**, 2089–2106.

Vecchi, G. A., and Coauthors, 2014: On the seasonal forecasting of regional tropical cyclone activity. *Journal of Climate*, **27 (1)**, 7994–8016.

Wheeler, T., and J. von Braun, 2013: Climate change impacts on global food security. *Science*, **341 (6145)**, 508–513.

Wills, R. C., and T. Schneider, 2018: Mechanisms setting the strength of orographic rossby waves across a wide range of climates in a moist idealized gcm. *Journal of Climate*, **31 (18)**, 7679–7700.

Wilson, C., and R. G. Williams, 2006: When are eddy tracer fluxes directed downgradient? *Journal of Physical Oceanography*, **36 (23)**, 189–202.

LIST OF TABLES

TABLE 1. Variance of December-January-February (DJF) 850hPa synoptic temperature over Eurasia (40°E-120°E and 30°N-75°N) and North America (240°E-280°E and 30°N-75°N) in the FLOR simulations and observed variances from 1979-2012. All units are K^2 and the plus/minus values show the standard deviations of the interannual variability.

	MERRA reanalysis 1979-2012	Control	no-Tibet	no-Rockies
North America	15.7 ± 2.6	18.1 ± 2.4	19.4 ± 2.7	16.8 ± 2.9
Eurasia	8.6 ± 2.0	12.6 ± 2.3	14.0 ± 2.8	12.4 ± 2.2
Difference	7.1	5.5	5.4	4.4

LIST OF FIGURES

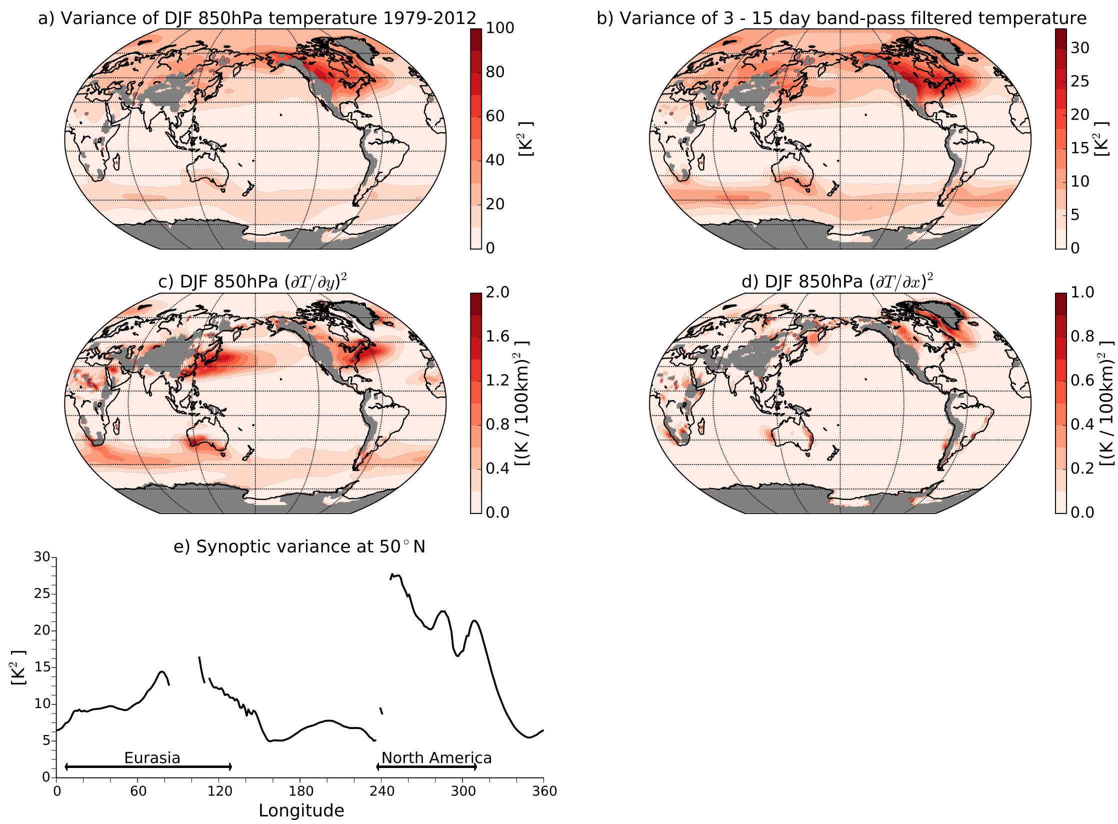

FIG. 1. a) Variance of December-January-February (DJF) 850hPa daily temperature for the period 1979 to 2012, calculated using data taken from the MERRA reanalysis dataset. Locations where topography intrudes through 850hPa are masked in gray. b) Same as panel a, but the data are filtered using a fourth-order Butterworth filter to only retain power at synoptic time-scales, here defined as 3 to 15 days. c) Climatological DJF squared meridional temperature gradients for the same data. d) Climatological DJF squared zonal temperature gradients for the same data. e) Profile of synoptic-scale 850hPa temperature variance at 50°N. Gaps in the profiles show where topography intrudes into the 850hPa level.

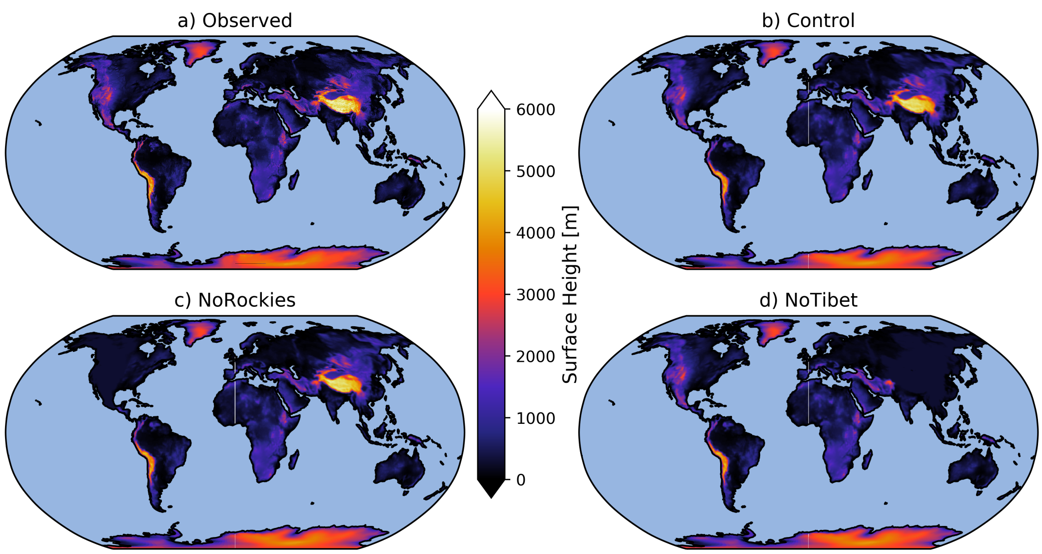

666 FIG. 2. a) Observed topography of Earth, taken from the ETOPO5 dataset, with 5 minute resolution. b) Topography in the control simulation of FLOR. c) Topography in the no-Rockies simulation. d) Topography in the no-Tibet simulation.

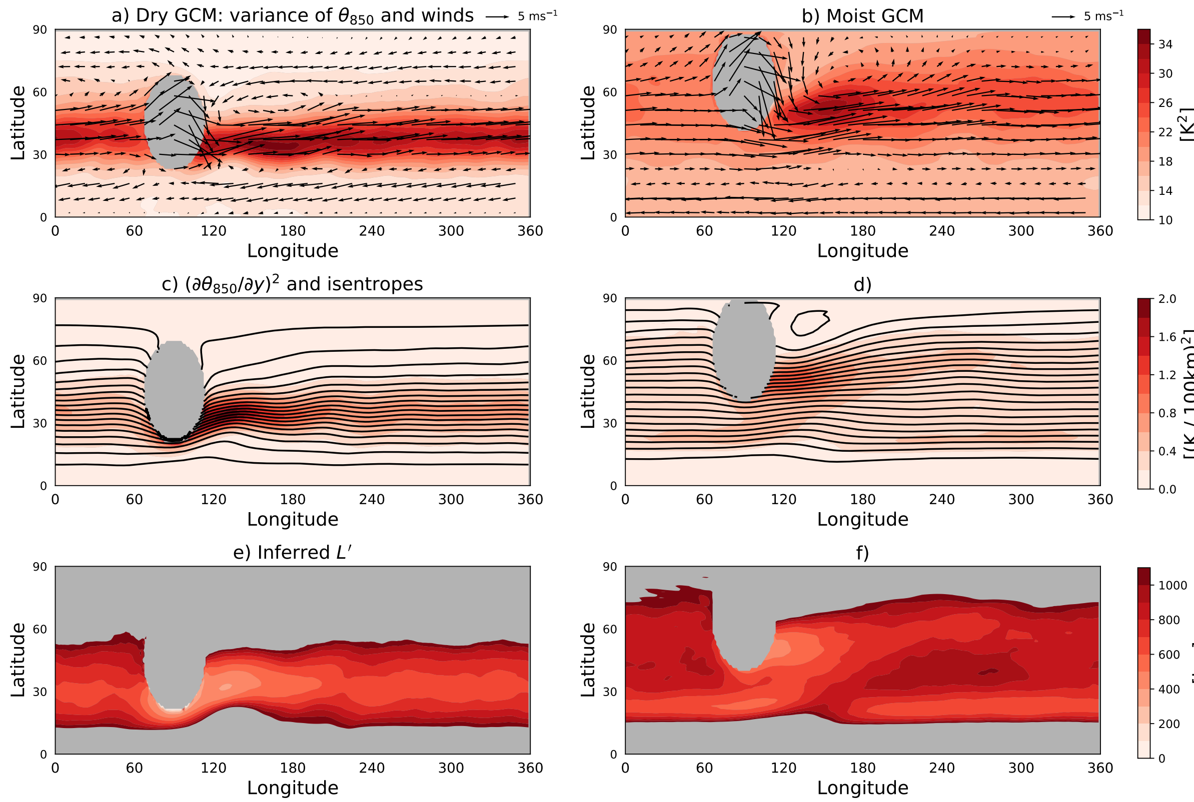

FIG. 3. a) Variance of synoptic (3 to 15 days) 850hPa potential temperature (contours) and total wind vectors (arrows) in a simulation with the dry GCM and maximum orographic height of 4km. b) Same as panel a) but for the simulation with the moist GCM with 4km orography. c) Squared meridional gradient of time-averaged potential temperature (colored contours) and isentropes (black contours, with contour interval 2K) at 850hPa for the same simulation as in panel a). d) Same as panel c) but for the simulation with the moist GCM with 4km orography. e) Inferred mixing length L' for the simulation with the dry GCM and maximum orographic height of 4km. f) Same as panel d) but for the simulation with the moist GCM with 4km orography. In all panels gray indicates locations with surface pressure less than 850hPa or, in the bottom panels, where values are outside the colorbar range. In a) and b) the winds are taken from the 0.85-σ level so that the flow over and around the orography is visible.

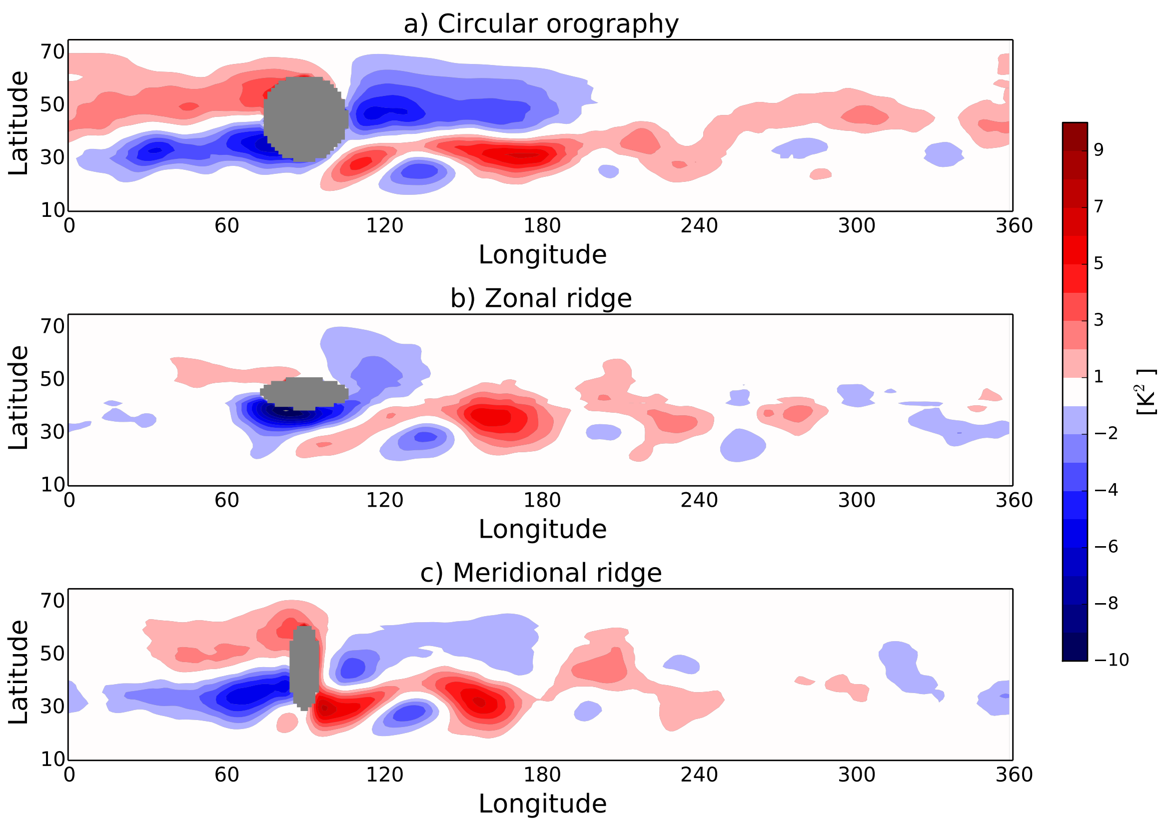

679 FIG. 4. a), b), c) Zonal anomalies in the variance of synoptic (3-15 day) 850hPa potential temperature in the
680 dry GCM simulations with H = 4km and the circular Gaussian orography (a, $\alpha = \beta = 15^\circ$), the zonal ridge (b,
681 $\alpha = 5^\circ$ and $\beta = 15^\circ$) and the meridional ridge (c, $\alpha = 15^\circ$ and $\beta = 5^\circ$).

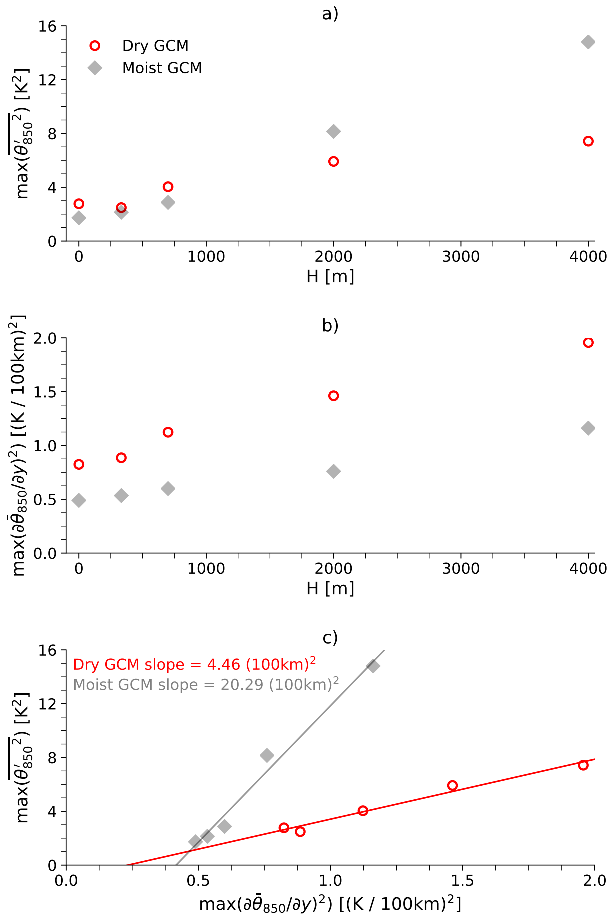

FIG. 5. a) Maximum anomalous 850hPa potential temperature variance (max($\overline{\theta'^2_{850}}$)) as a function of mountain height, H, in the simulations with the dry GCM (red circles) and with the moist GCM (gray diamonds). max($\overline{\theta'^2_{850}}$) is calculated as the maximum zonal anomaly in 850hPa potential temperature variance in the 120° downstream of the peak of the orography. b) Maximum zonal anomaly of the squared meridional potential temperature gradient at 850hPa (max($(\partial\bar{\theta}_{850}/\partial y)^2$)) as a function of H in the simulations with the idealized GCMs. max($(\partial\bar{\theta}_{850}/\partial y)^2$) is calculated as the maximum zonal anomaly in the 850hPa meridional potential temperature gradient in the 120° downstream of the peak of the orography. c) max($\overline{\theta'^2_{850}}$) versus max($(\partial\bar{\theta}_{850}/\partial y)^2$) in the simulations with the idealized GCMs. The lines show linear least-squares fits to the two sets of simulations.

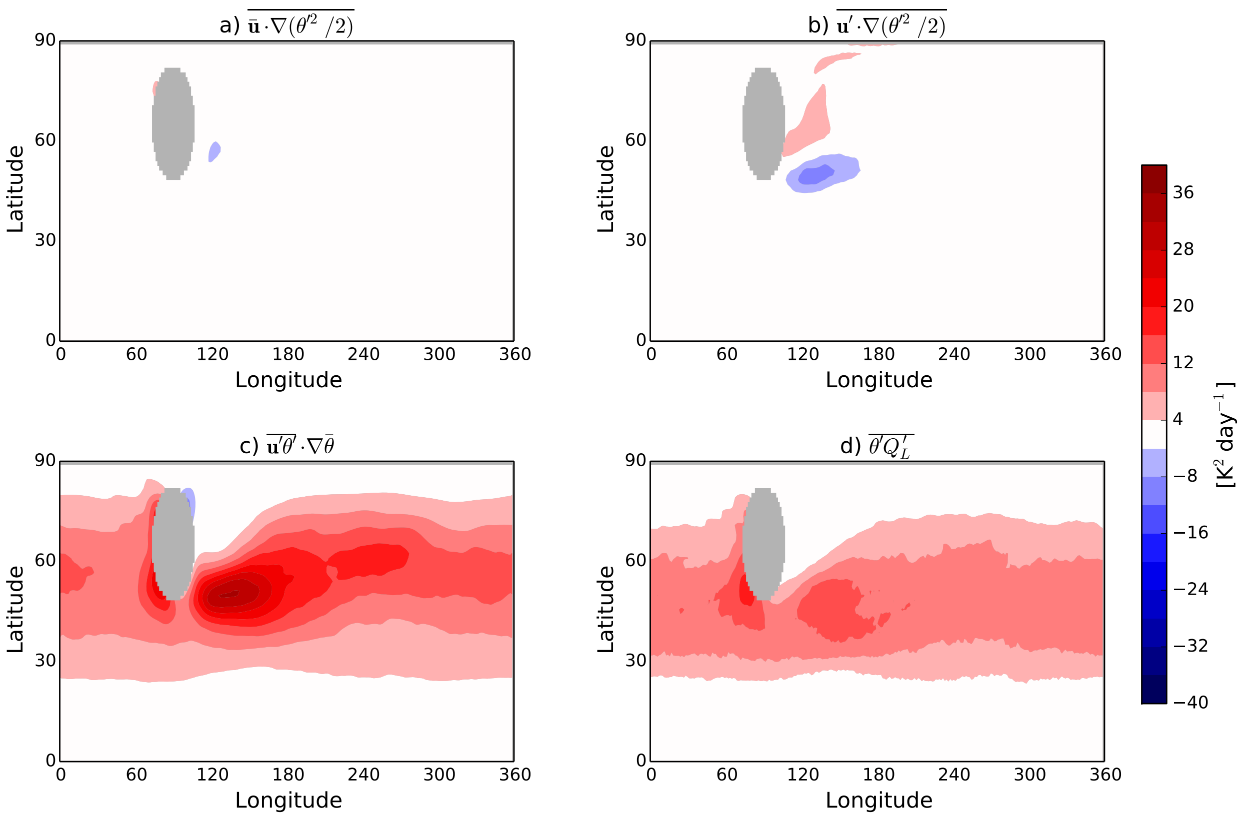

FIG. 6. Panels a), b) and c): advective terms in the 850hPa potential temperature variance budget from a simulation with the moist GCM and a mountain height of 4km. Locations where topography intrudes through 850hPa are masked in gray. Panel d): the contribution of latent heating fluctuations to 850hPa potential temperature variance in the same simulation.

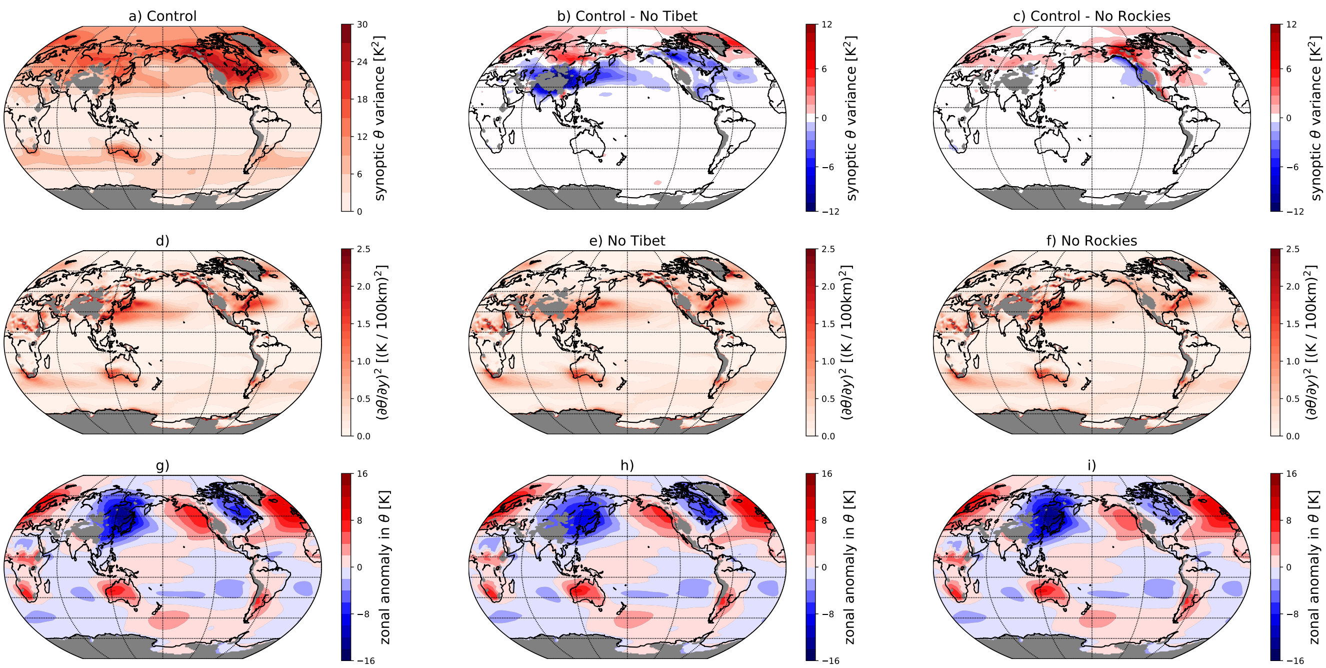

FIG. 7. a) Synoptic-scale variance of DJF 850hPa potential temperature in the control simulation with the comprehensive climate model, FLOR. b) Difference in synoptic-scale variance between the control simulation and the no-Tibet simulation. c) Difference in synoptic-scale variance between the control simulation and the no-Rockies simulation. d) DJF squared meridional potential temperature gradients in the control simulation. e) DJF squared meridional potential temperature gradients in the no-Tibet simulation. f) DJF squared meridional potential temperature gradients in the no-Rockies simulation. g), h), i) DJF zonal anomalies in 850hPa potential temperature in the same simulations. Locations where topography intrudes through 850hPa are masked in gray.

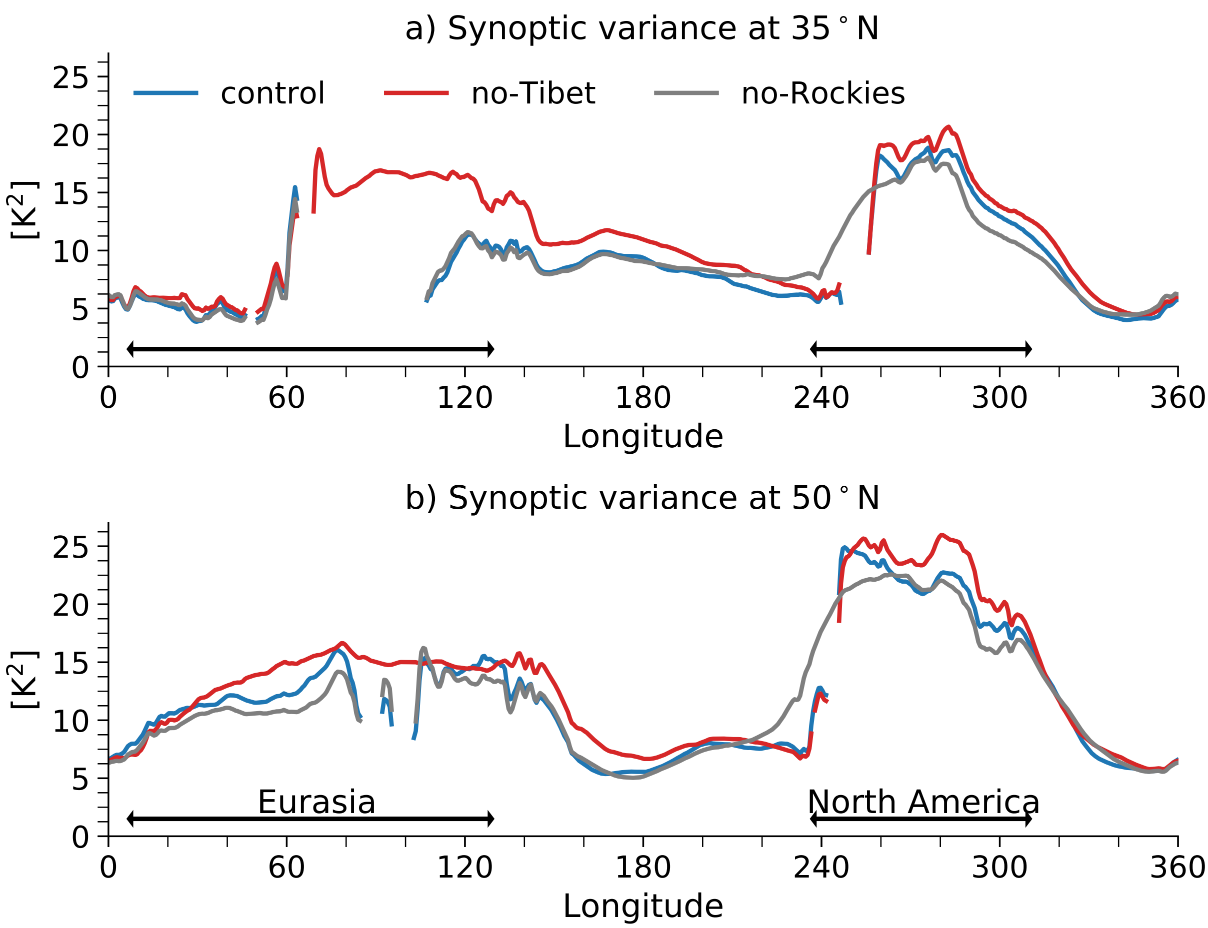

FIG. 8. a) Profiles taken at 35°N of synoptic-scale variance of DJF 850hPa potential temperature in the three simulations with FLOR. b) Profiles taken at 50°N. Gaps in the profiles show where topography intrudes into the 850hPa level.

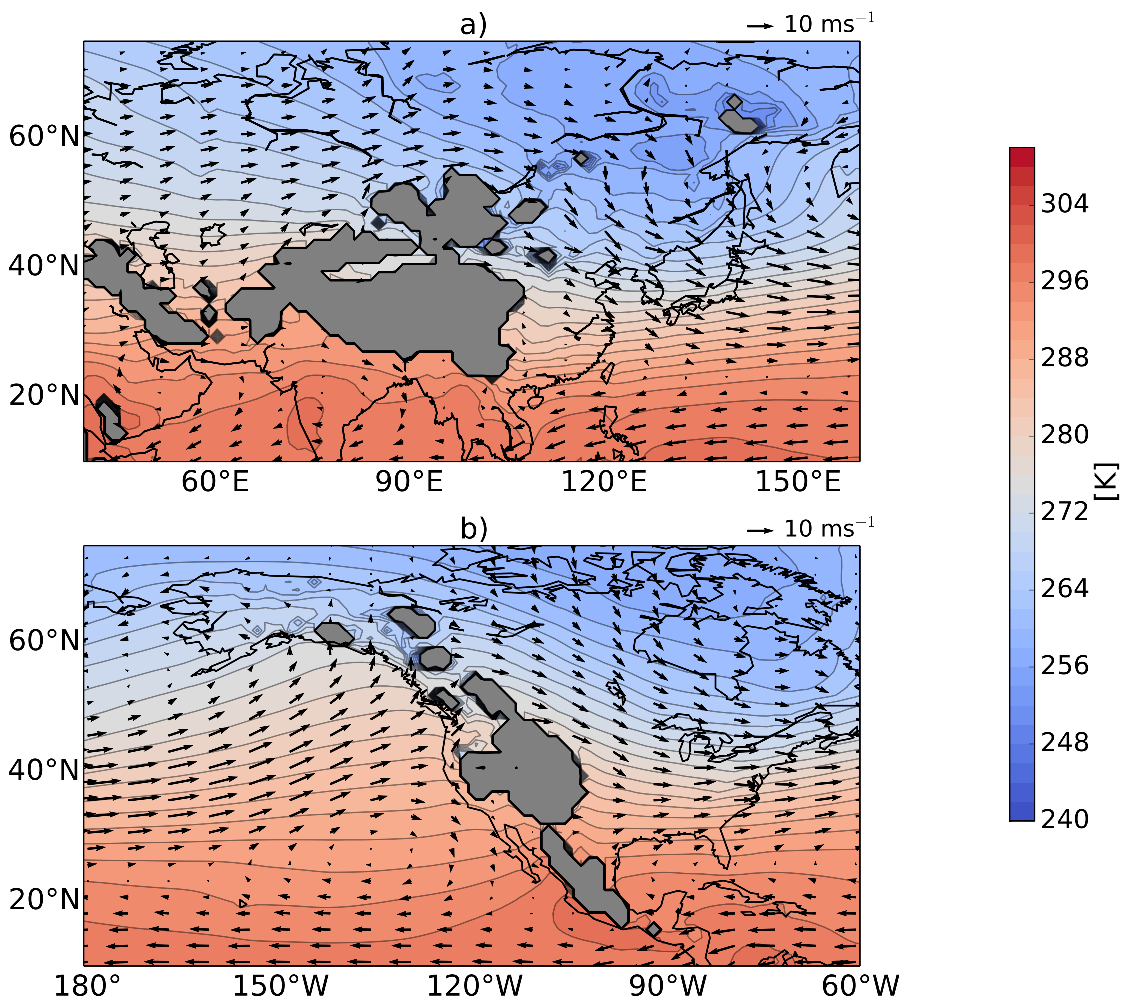

704 FIG. 9. a) DJF 850hPa temperature (contours) and total wind vectors in the vicinity of the Tibetan Plateau, averaged over the period 1979 to 2012. Data are taken from the MERRA reanalysis dataset. Locations where topography intrudes through 850hPa are masked in gray. b) Same for the region near the Rocky Mountains.

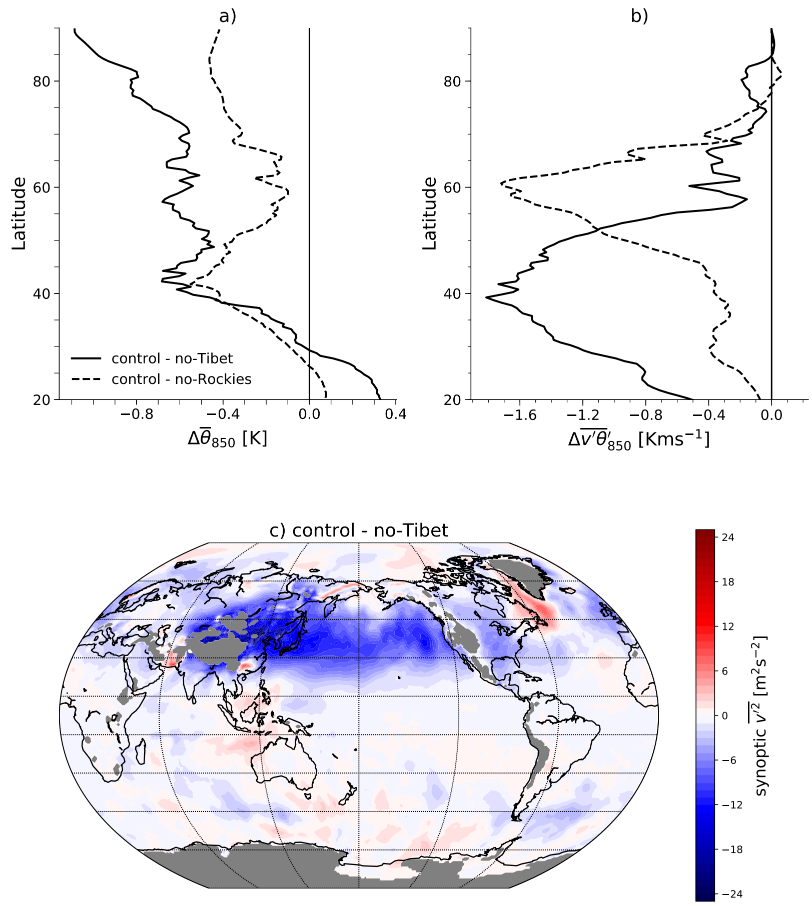

FIG. 10. a) Difference in zonal-mean θ_{850} between the control simulation with FLOR and the no-Tibet simulation (solid line) and difference between the control simulation and the no-Rockies simulation (dashed line). b) Differences in transient eddy potential temperature flux in the same simulations. c) Difference in DJF synoptic 850hPa eddy kinetic energy ($\overline{v'^2}$) between the control simulation and the no-Tibet simulation.

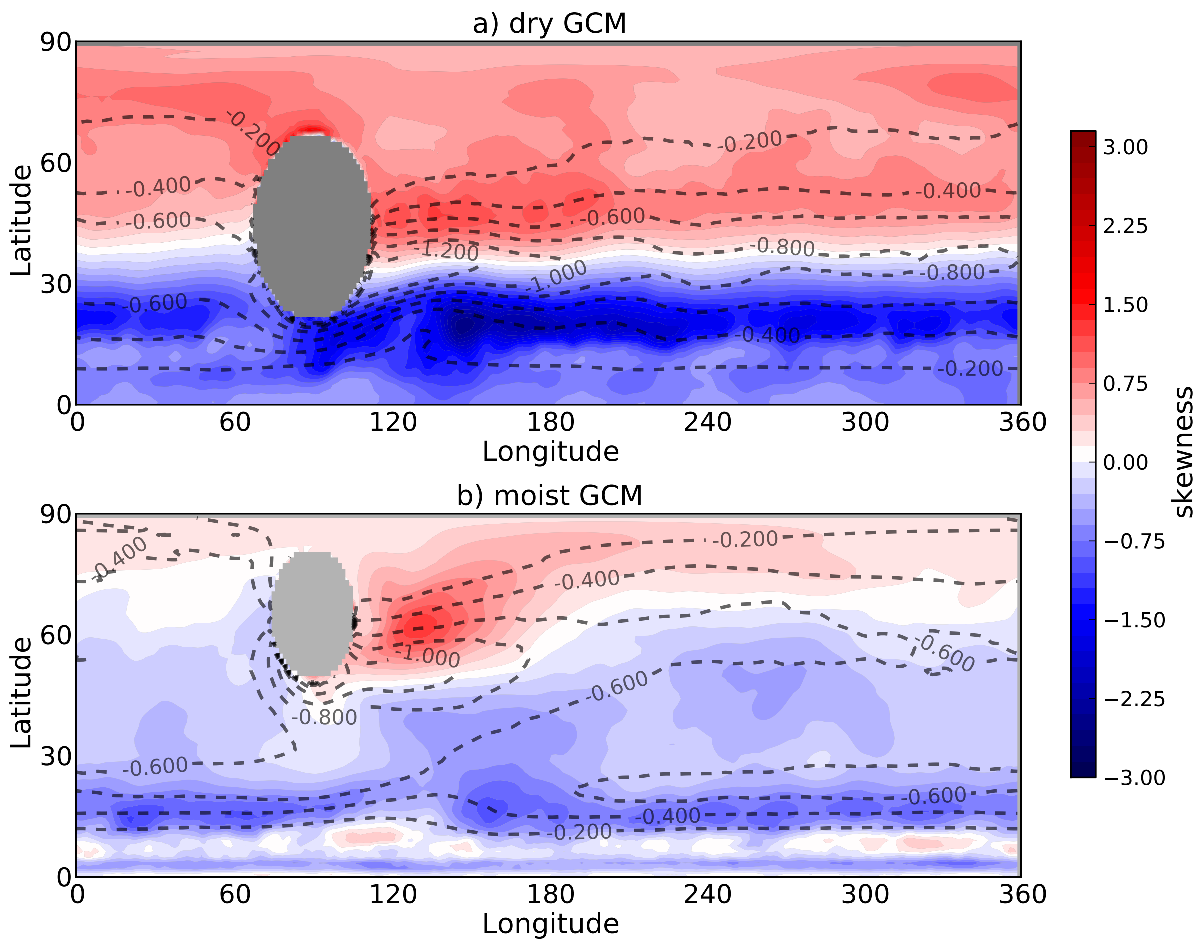

711 FIG. 11. a) Skewness of 850hPa synoptic temperatures (colored contours) and 850hPa meridional temperature
712 gradients (black contours, contour interval = 0.2K(100km)$^{-1}$) in the dry GCM simulation with H = 4km. b)
713 Same for the simulation with the moist GCM. The meridional gradient contour interval is 0.2K/100km in both
714 panels.

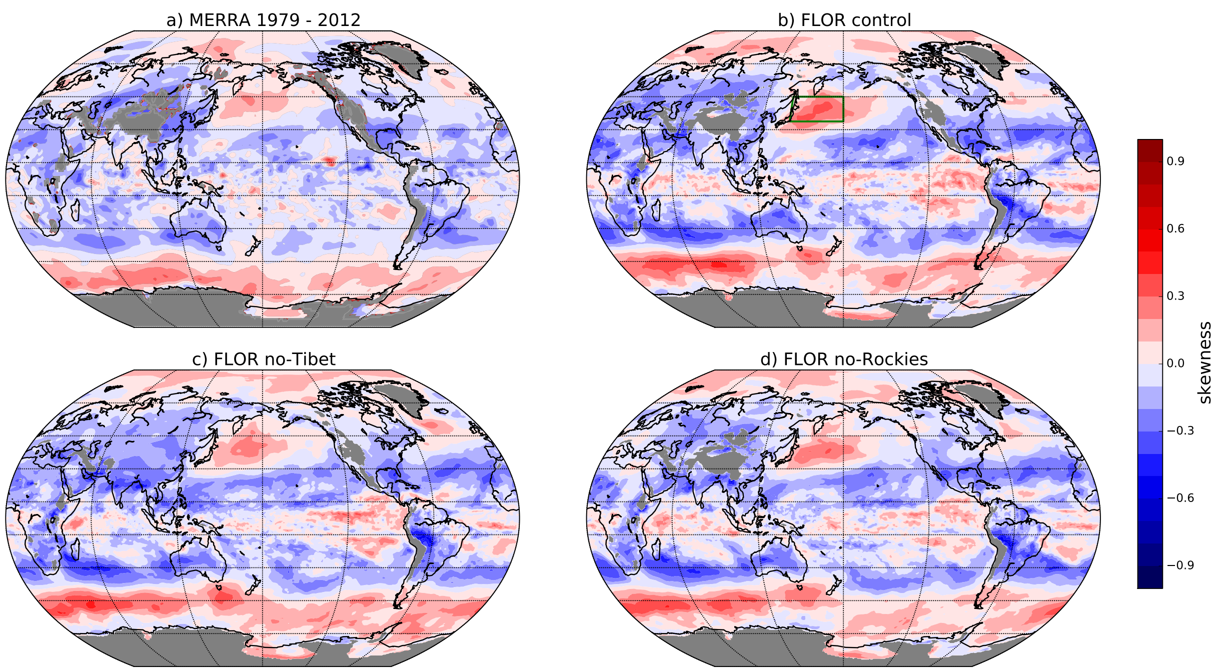

715 FIG. 12. a) Skewness of DJF 850hPa synoptic temperatures for the period 1979-2012 in the MERRA data.
716 b) Skewness of DJF 850hPa synoptic temperatures in the control simulation with FLOR. c) Skewness of DJF
717 850hPa synoptic temperatures in the no-Tibet simulation with FLOR. d) Skewness of DJF 850hPa synoptic
718 temperatures in the no-Rockies simulation with FLOR.